Nanoscale

COMMUNICATION

View Article Online
View Journal | View Issue

Cite this: *Nanoscale*, 2014, **6**, 10524

Received 17th June 2014
Accepted 7th July 2014

DOI: 10.1039/c4nr03300k

www.rsc.org/nanoscale

Conduction control at ferroic domain walls *via* external stimuli†

J. C. Yang,‡[a] C. H. Yeh,‡[b] Y. T. Chen,[c] S. C. Liao,[d] R. Huang,[e] H. J. Liu,[ac] C. C. Hung,[f] S. H. Chen,[f] S. L. Wu,[b] C. H. Lai,[d] Y. P. Chiu,[c] P. W. Chiu[b] and Y. H. Chu*[a]

Intriguing functionalities at nano-sized domain walls have recently spawned a new paradigm for developing novel nanoelectronics due to versatile characteristics. In this study, we explore a new scenario to modulate the local conduction of ferroic domain walls. Three controlling parameters, *i.e.*, external electrical field, magnetic field and light, are introduced to the 90° domain walls (90° DWs) of $BiFeO_3$. Electrical modulation is realized by electrical transport, where the mobility of 90° DWs can be altered by gating voltage. We further use the ferromagnetic/antiferromagnetic coupling to reveal the inherent magnetism at the DWs. With an established magnetic nature, magnetotransport has been conducted to introduce magnetic controlling parameter, where a giant positive magnetoresistance change can be observed up to 200%. In addition, light modulated conduction, a core factor for multifunctional applications, is successfully demonstrated (current enhancement by a factor of 2 with 11 W white lamp). These results offer new insights to discover the tunability of domain wall nanoelectronics.

Introduction

Demand for small electronic devices with multifunctionalities has arisen in the pursuit of fast information computation and communication. For numerous functional materials that are being proposed and explored, complex oxide interfaces have emerged as one of the most exciting systems because of their unique properties, and they offer new possibilities for next-generation electronic devices.[1–3] Recently, three types of complex oxide interfaces have been established,[4] namely, the heterointerfaces, tubular interfaces and homointerfaces. Interesting electronic transport behaviors have been discovered in these interfaces, including a highly mobile quasi-two dimensional electron gas formed between two insulators;[3,5] the local conduction observed at the tubular interfaces of $BiFeO_3$–$CoFe_2O_4$ (BFO–CFO) heterostructure[4] and domain walls (DWs) in ferro/multiferroics.[6–8] Therefore, for practical applications, it is desirable to gain further control of interface functionalities through external stimuli. Modulation of local conduction at heterointerface ($LaAlO_3$–$SrTiO_3$)[9–11] and BFO–CFO tubular interface were demonstrated recently.[12] However, the external control of domain wall (complex oxide homointerface) conduction is yet to be fully explored. Multiferroic BFO provides robust coupling between electricity and magnetism and the potential to manipulate one through the other.[13,14] The domain walls of BFO have suggested new possibilities to explore the interplays of magnetic and electronic characteristics at an interface.[15,16] In light of both scientific research and practical applications,[17] BFO DWs serve as potential candidates for next generation multifunctional electronic devices.

In this study, we take 90° DWs in BFO as a model homointerface to demonstrate that the conduction of domain walls can be modulated by external electric field, magnetic field, and light, as illustrated in Fig. 1(a). Epitaxial BFO thin films were prepared on $NdScO_3$(110) (NSO) substrate by pulsed laser deposition at 700 °C in oxygen at a pressure of 100 mTorr and cooled in 1 atm after deposition. The particular role of tensile strain has been used to stabilize the orthorhombic phase, in which the depolarization field suppresses the $\langle 111\rangle_{pc}$ polarizations of the BFO parent phase to $\langle 110\rangle_{pc}$ directions.[18] The boundaries of the two adjacent domains with $\langle 110\rangle_{pc}$ polarizations give rise to the 90° DWs in BFO. However, to build a model 90° DWs platform, we applied proper anisotropic strain provided by orthorhombic NSO substrate to exclude two possible structure variants, which resulted in periodic 90° DWs.

[a]*Department of Materials Science and Engineering, National Chiao Tung University, Room 709, Engineering Building VI, 1001 University Road, Hsinchu, 30010, Taiwan. E-mail: yhc@nctu.edu.tw; Tel: +1-510-501-9307*

[b]*Institute of Electronics Engineering, National Tsing Hua University, Hsinchu, 300, Taiwan*

[c]*Department of Physics, National Sun Yat-sen University, Kaohsiung 80424, Taiwan*

[d]*Department of Materials Science and Engineering, National Tsing Hua University, Hsinchu, 300, Taiwan*

[e]*Key Laboratory of Polar Materials and Devices, Ministry of Education, East China Normal University, Shanghai 200062, China*

[f]*ThinTech Materials Technology Co., Ltd., Kaohsiung, 82151, Taiwan*

† Electronic supplementary information (ESI) available. See DOI: 10.1039/c4nr03300k

‡ These authors contributed equally in this work.

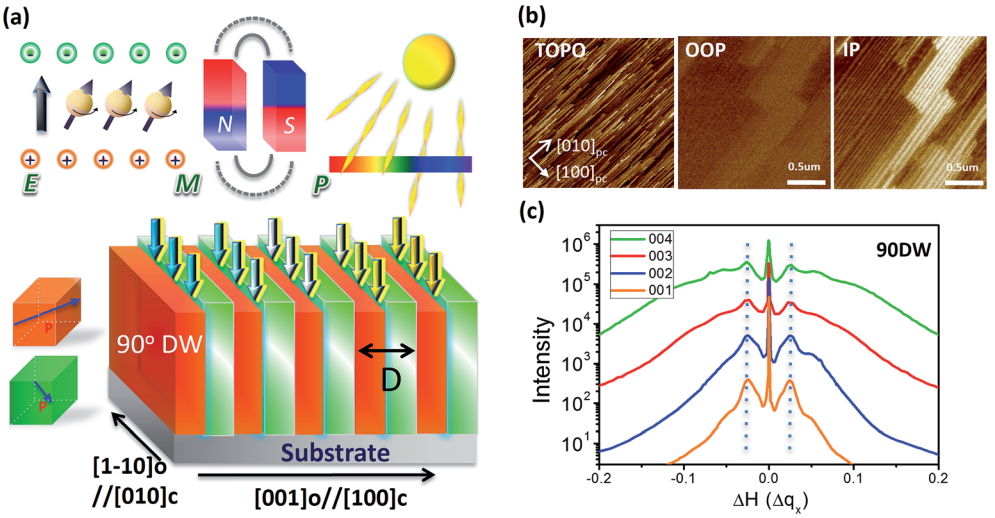

Fig. 1 (a) Schematic for the modulation of local conduction of 90° domain walls in $BiFeO_3$ *via* electrical, magnetic as well as photonic tuning factors. The orange and green patterns represent $BiFeO_3$ domains with respect to different polarizations, where a homointerface domain wall emerges at the boundary of the two distinct domains. (b) The topography, in-plane and out-of-plane piezoforce response microscopy images of 90° DW sample. The images were probed with the scanning cantilever along the $[100]_{pc}$ direction (c) high-resolution X-ray H-scans of 90° DW thin films.

Results and discussion

The key features of periodic 90° DWs were distinguished by a combination of piezoresponse force microscopy (PFM) and X-ray diffraction. The topography and ferroelectric domain patterns of 90° DWs were imaged by atomic force microscope and PFM, respectively, as shown in Fig. 1(b). The long-range elastic interaction and structural nature give rise to topography in polar materials. A lateral lamellar morphology is discovered in 90° DW BFO, in which the elastic relaxation and lattice structure lead to surface reconstruction, resulting in planar topography.[18] Three strong contrasts (bright, dark and brown) in the in-plane (IP) PFM image with scanning tip cantilever along the $[100]_{pc}$ direction together with a negligible response of the out-of-plane (OOP) PFM image were observed. These PFM results confirmed the $\langle 110\rangle_{pc}$ polarization of the BFO/NSO sample, which is the fundamental building unit to construct the periodic 90° DWs in BFO. Furthermore, the PFM results unveiled the periodic feature of 90° domain patterns with $\{001\}_{pc}$ domain boundaries.

X-ray diffraction serves as an ideal tool to determine the periodicity of the patterns. Thorough q_x-scans are executed with the X-ray parallel to $[001]_o/[100]_{pc}$ direction. Constant spacing in the q_x-scans from $(001)_{pc}$ to $(004)_{pc}$ are observed, as shown in Fig. 1(c). In q_x-scans, the tilting of the crystal structure of BFO gives rise to increasing splitting from $(001)_{pc}$ to $(004)_{pc}$ scans, whereas the reflections of periodic planar domain result in constant splitting in q_x-scans. In 90° DWs BFO, the planar domains formed by orthorhombic BFO phase result in constant spacing in the q_x-scans from $(001)_{pc}$ to $(004)_{pc}$. As a result, the domain spacing could be extracted by the Williamson–Hall plot,[19] in which the interception of the Williamson–Hall plot (not shown here) gives rise to a 15 nm periodic satellite reflection of periodic domain patterns, as marked in Fig. 1(a). Such a result is consistent with the value extracted from the PFM study. It is these periodic domain patterns that enable us to build a model system to facilitate the experimental setup and to quantize the conduction characteristics.

The well-aligned domain architectures were directly imaged *via* a spherical aberration corrected scanning transmission electron microscope (Cs-corrected STEM). A typical high angle annular dark-field (HAADF) STEM image obtained from the cross-sectional sample is shown in Fig. 2(a). It reveals that the interface between the BFO thin film and the NSO substrate is atomically flat and the lattices perfectly match up to each other. Mismatch dislocations and other defects were not observed. Fe ions shifted to the middle-left in the Bi rectangles in the BFO thin film, indicating that polarization direction is along the $\langle 110\rangle_{pc}$. Two 90° DWs with discernable lattice distortion were imaged, as labeled in between the two red dotted lines in Fig. 2(a).

To explore the local electronic environment at the domain walls, we used scanning tunneling microscopy (STM) to determine the electronic structure across the 90° DWs. In the present STM measurements, the sample was cleaved in the STM chamber *in situ* to obtain the cross-sectional slice of domain patterns, as shown schematically in Fig. 2(b). All the STM experiments reported here were performed in an UHV chamber with a base pressure of approximately 5×10^{-11} Torr. Our STM and scanning tunneling spectroscopy (STS) studies provide direct experimental evidence of the nature and origin of the electronic conductivity at 90° DWs in BFO. The local electronic density of states (DOS) at each site was determined from the first derivative of the tunneling current with respect to the sample bias (dI/dV). The electronic image in Fig. 2(b) recorded the spatial dependence of the tunneling current at −2.1 V in the

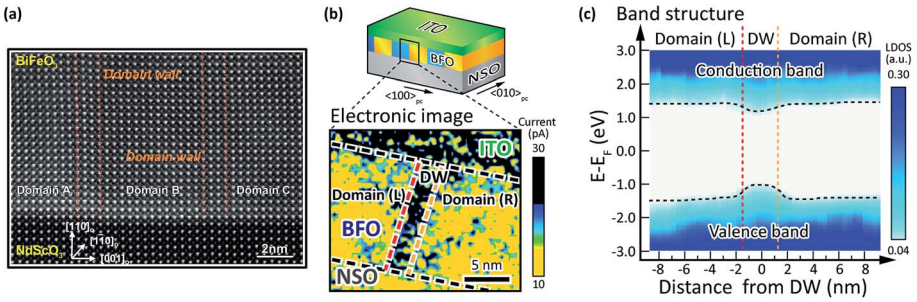

Fig. 2 (a) HAADF STEM image of 90° domain walls in $BiFeO_3/NdScO_3$ thin film in a cross-sectional view, where the location of the domain walls are labeled in between two red dotted lines. (b) The experimental architecture of the 90° domain wall sample for cross-sectional scanning tunneling microscopy (upper side) and the spatial dependence of the tunneling current at −2.1 V in the vicinity of the domain wall in BFO (downward side). The ITO protection layer has been deposited as the scanning buffer and the location reference. (c) The band structure constructed by the first derivative of the tunneling current with respect to the sample bias (d*I*/d*V*) in the electronic mapping scan.

vicinity of the domain wall in BFO. The variations of the tunneling current characteristics reveal distinct electronic properties across the domain wall, involving a decrease in the local band gap and built-in asymmetric potential barriers at the domain walls. When analyzed layer-by-layer, d*I*/d*V* curves can clearly address the characteristics of electrostatic potential steps across the domain wall. In Fig. 2(c), with the characteristics of d*I*/d*V* curves, the atomic-scale evolution of the local electronic property across the domain wall can be quantitatively depicted and directly traced. The visualized atomic-scale band alignment provides a direct observation of how the band structures evolve across the domain wall. The key feature is that the change in band gap is attributed to the shift of current onset at both the positive and negative sample bias. The obvious downward shift in the conduction-band edge and an upward shift in the valence-band edge can be correlated with the Fe–O octahedral deformations and the surroundings of O 2p-Fe 3d states in the wall region.[16] This finding of a significant reduction in the electronic bandgap suggests the promising conduction scenario of 90° DWs, which is a new type of multiferroic domain wall in BFO.

To explore electrical control on the conduction of 90° DWs, we fabricated the three-terminal test architecture, as shown in Fig. 3(a). In this test structure, transport measurements as functions of temperature, magnetic field, and gate voltage have been carried out. Three types of device configurations, as shown in the cartoons in Fig. 3(b), were prepared for the study on the conduction of 90° domain walls. As shown in Fig. 3(b), electrical conduction is only observed in devices with electrodes aligned perpendicular to the domain walls (device A and B). The device with longer electrodes (device A) is connected to more domain walls, and hence shows higher conduction. The absence of electrical conduction in device C as well as the higher conduction of device A clearly indicates that domain walls give rise to the charge conduction. We further investigated the electric-field gating effects on domain wall conduction using three-terminal devices with top-gate geometry (as illustrated by the cartoon in Fig. 3(a)). Note that the application of gate voltage did not alter the direction of ferroelectric polarization of the domains underneath the gate electrode because no bottom electrode is used. The domain walls remained intact throughout the measurements. As shown in Fig. 3(c), the results of the field-effect transport at room temperature show significant increases in conduction at domain walls when applying positive gate bias, revealing n-type conduction at the 90° DWs. The observed n-type conduction and activation energy found on temperature dependent experiments (see ESI†) suggested that electron chemical doping resulted from oxygen vacancies at and/or surrounding the domain walls, which are in good agreement with the previous studies.[8,15] As a result, the observed enhanced conduction can be understood by an electronic conduction mechanism, which is driven by a local change in the bandgap as a result of discontinuity in in-plane polarizations and local defect chemistry. Further information buildup with the top-gate geometry yields carrier mobility values of ~1.6–1.8 $cm^2\ V^{-1}\ s^{-1}$ at a source–drain electric field of 8 kV cm^{-1} with a gate voltage dependence, as shown in Fig. 3(d). For practical applications in high-density information communication and low-energy consumption, one can significantly enhance carrier density *via* divalent-ion doping;[20] the advanced modification of domain wall conductivity will be revealed elsewhere. These results have clearly elucidated the ability for tuning carrier transport *via* external electrical fields.

To achieve magnetic modulation, a detailed understanding of the magnetic state of 90° DWs is required because the conduction of the BFO domain walls was predicted to be highly correlated between the free carriers, electronic structures, and the local spin states at the walls.[16] The magnetic anisotropy of 90° DWs is probed by the ferromagnetic–antiferromagnetic exchange coupling with Permalloy ($Ni_{81}Fe_{19}$, Py) layer. We deposited 5 nm thick Py layer on BFO under a magnetic field of 120 Oe along $[1{-}10]_o/[010]_{pc}$ and $[001]_o/[100]_{pc}$ directions, and the corresponding magnetic hysteresis loops are shown in Fig. 4(a) and (b), respectively. For samples with deposition field along $[1{-}10]_o/[010]_{pc}$ direction, *i.e.* along the DWs, a typical exchange-biased loop[21] with a bias field (H_{eb}) of 10 Oe is observed when measuring along the deposition field; whereas a hard-axis loop with an anisotropy field (H_k) of 50 Oe is obtained when measuring along directions that are perpendicular to the deposition field. A similar phenomenon has been revealed in a previous study.[22]

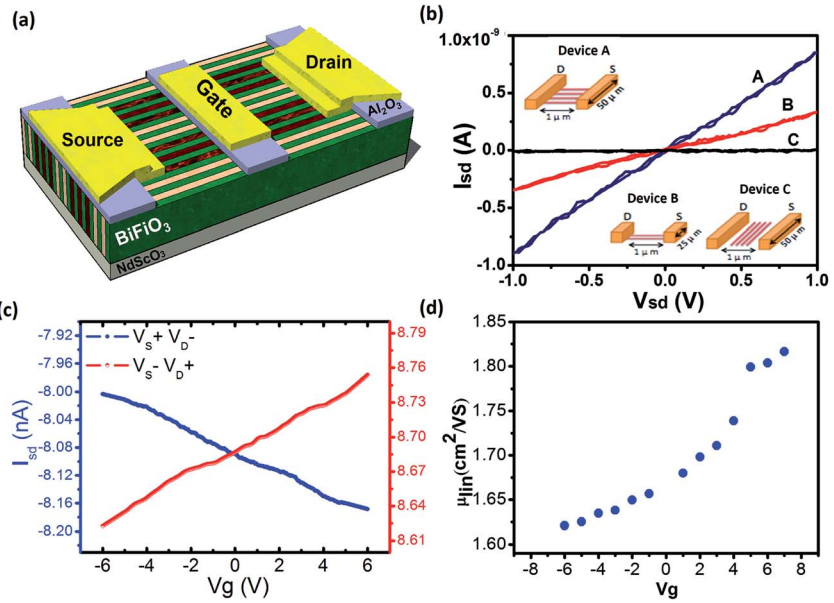

Fig. 3 (a) Experimental configuration of three-terminal 90° domain wall devices with top-gate geometry. (b) The current–voltage curves with respect to the three types of device configurations. Device A with 50 μm long source–drain electrodes that are aligned perpendicular to the domain walls, device B with 25 μm long source–drain electrodes that are aligned perpendicular to the domain walls, and device C with 50 μm long source–drain electrodes that are aligned parallel to the domain walls. (c) The gating effects of the 90° domain walls. The blue and red curves represent the measurements with identical but reverse electrical potentials of $V_{sd} = 8$ V and $V_{sd} = -8$ V, respectively. (d) Carrier mobility as a function of gate voltages extrapolated at an electric field of 8 kV cm^{-1} across the source and drain electrodes.

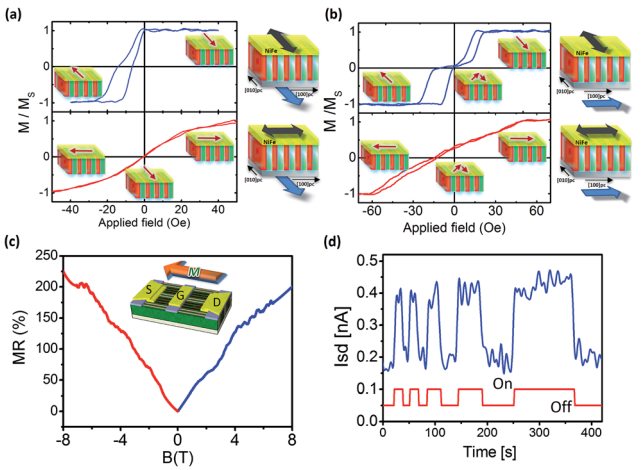

Fig. 4 (a and b) Exchange coupling study of 90° domain walls and ferromagnetic Permalloy ($Ni_{81}Fe_{19}$, Py) top layers. 5 nm thick Py layers were deposited on $BiFeO_3$ with an applied magnetic field of 120 Oe along the $[1{-}10]_o/[010]_{pc}$ and $[001]_o/[100]_{pc}$ directions. The M – H loops are measured parallel and perpendicular to the deposited fields, as illustrated in the cartoons. (c) Magnetotransport measurement as a function of magnetic field. The magnetic field is applied parallel to electron transport direction. (d) The photonic response of 90° domain walls. The on-off states of the photo pulses are depicted in the red curve, while the blue curve shows the current variation along with photo pulses.

These results indicate that the coupling between BFO and Py creates an easy axis and a bias field, which are parallel to the deposition field direction. However, the sample with deposition field along $[001]_o/[100]_{pc}$ shows abnormal and interesting behaviors; the loop measured along $[001]_o/[100]_{pc}$ showed the an H_{eb} of 13 Oe and shape of a hard-axis loop with an H_k of 50 Oe. On the other hand, the loop measured along $[1{-}10]_o/[010]_{pc}$ showed a double-shifted feature, two easy-axis loops with opposite H_{ex} of 13 Oe. Based on these findings, we may conclude that the deposition field along $[001]_o/[100]_{pc}$ direction would create a bias field that lies at $[001]_o/[100]_{pc}$, and an easy axis lies along $[1{-}10]_o/[010]_{pc}$. In other words, exchange coupling between Py and 90° DWs BFO would always create an easy axis parallel to $[1{-}10]_o/[010]_{pc}$ regardless the direction of the deposition field. This phenomenon is attributed to the intrinsic anisotropy of uncompensated spins in 90° DWs BFO. Another indication based on this observation is the collinear coupling between the uncompensated spins and the spin of Py because the perpendicular coupling would not create exchange bias in similar systems.[23] For deposition field applied along $[001]_o/[100]_{pc}$, a part of the uncompensated spins rotates to the $[001]_o/[100]_{pc}$ and forms the exchange bias along $[001]_o/[100]_{pc}$, whereas the other part of spins do not rotate and form an easy axis along $[1{-}10]_o/[010]_{pc}$. Most of the uncompensated spins in BFO pin the spins of Py at the $[001]_o/[100]_{pc}$ axis and only a certain part of the uncompensated spins rotate and couple collinearly with spins in Py within this feature, resulting in a bias field that is parallel to the deposition field. Despite the exchange coupling mechanism being unclear, it is believed that magnetic spins at the walls are highly correlated to the strain states and the direction of the adjacent ferroelectric dipoles.[15,22] Such results have given hints to control the local conduction with external magnetic stimulation.

The entangled multiferroic orders of BFO thin films enable us to integrate the magnetic and electronic control parameters. To achieve this, high-field magnetotransport of the 90° DWs is studied using the charge transport with in-plane magnetic field parallel to the domain walls, as illustrated in Fig. 4(c). It is striking to observe the non-trivially high (~200% at 8 T) and positive magnetoresistance in such a periodic domain wall array. A scenario based on multilayer magnetic coupling is proposed to explain the positive magnetoresistance. Assuming that the canted spin at the domain wall forms ferromagnetic clusters, whose polarization is aligned to the external magnetic field, the conduction through these ferromagnetic clusters (*i.e.* the magnetoresistance) depends on the coupling between the clusters, resulting in either negative magnetoresistance when ferromagnetically coupled, or positive magnetoresistance when anti-ferromagnetically coupled. This scenario is similar to the proposed model for the giant positive magnetoresistance effect observed in multilayer devices.[24,25] If this scenario applies, the observed large positive magnetoresistance implies the anti-ferromagnetic coupling in canted spin cluster at the 90° domain walls. However, more studies are required and are being undertaken for explaining the details regarding the transport mechanism behind the non-trivial magnetoresistance.

In addition to magnetic and electric tuning factors, we have explored light as an additional route to create multi-conduction states in the device. An 11 W white lamp with continuous wavelength has been used as the light source. Remarkably, the conduction current doubles as light is shone on the device, as shown in Fig. 4(d). The well-aligned domain patterns create a built-in potential across the domain walls, which give rise to an enhanced charge separation and a higher photovoltaic voltage.[26] The photo-response is related to the band gap of BFO thin film, and the local band gap drop across the domain walls. More free carriers are excited when exposed to light. Then, the charge separation is achieved by the local ferroelectric polarizations, resulting in the increased conduction level. Furthermore, the sensitive responses along with light irradiation suggested a higher photo current when constructing a photovoltaic device. We have demonstrated the experiment to introduce the photonic controlling parameter for modulating the local conductivity of the homointerfaces. Furthermore, it is remarkable that the DW width is only merely ~2 nm according to our previous study,[27] indicating the promising size feature of potential applications. Our finding has once again highlighted the intriguing multifunctionalities of such homointerfaces.

Conclusions

In summary, we have demonstrated the modulation of the local conduction of 90° DWs in BFO thin film *via* external stimuli, namely electronic, magnetic as well as light tuning factors. X-ray diffraction, piezoresponse force microscopy and transmission electron microscopy have provided the general features of the 90° DWs. Scanning tunneling microscopy has indicated a change in local band gap at the walls, which served as the conduction origin of the domain walls. We examined the magnetic structure in 90° DW through ferromagnetic/antiferromagnetic exchange coupling. Spin flop and uncompensated spin across the walls are highly correlated to the local ferroelectric polarization, which suggests a promising magnetic modulation of the local conduction. Magnetotransport has been conducted to integrate the magnetic and electronic parameters, where a giant positive magnetoresistance change is observed when applying an external field parallel to current and 90° DWs. We also provide a promising feature to include photo-response as an additional controlling factor: the sensitive and increased conduction change suggesting a new route for pursuing new photovoltaic device and multiple digit computation. Our results have offered a new perspective to control local conduction in ferroic domain walls with various stimuli, which shed light on constructing multi-functionalities and potential applications of nano-sized homointerfaces.

Experimental section

Sample fabrication

Epitaxial $BiFeO_3$ thin films were fabricated on (110) oriented $NdScO_3$ (NSO) single crystal substrate *via* pulsed laser deposition (PLD) with a KrF ($\lambda = 248$ nm) excimer laser. Pulsed laser beam was focused on $BiFeO_x$ ceramic target with an energy density of 3 J cm^{-2} and a repetition rate of 10 Hz. Samples were deposited on the substrate temperature of 700 °C and with 100 mTorr oxygen pressure. Samples were cooled to room temperature in an oxygen pressure of 1 atm. The ferromagnetic/antiferromagnetic bilayer samples were prepared by depositing 5 nm thick $Ni_{81}Fe_{19}$ with 5 nm Ta capping layer on BFO layer. Both the layers are deposited by magnetron sputtering with a base pressure of 5×10^{-8} Torr at room temperature. A magnetic field of 120 Oe was applied during the deposition to set the direction of exchange coupling.

Characterization of structure and physical properties

Surface morphology (AFM) and piezoresponse force microscopy (PFM) were performed using Bruker Multimode VIII. High-resolution X-ray diffraction techniques were employed to examine the crystal quality and domain spacing of $BiFeO_3$ (BFO) thin films at beamline BL17A in the National Synchrotron Radiation Research Center (NSRRC), Taiwan. The BFO heterostructure was characterized by a Cs-corrected HAADF-STEM (STEM; JEOL JEM2100F, Cs-corrector; CEOS Gmbh). In the present scanning tunnelling microscopy (STM) measurements, the sample was cleaved in the STM chamber *in situ* to obtain the cross-sectional slice of the BFO heterostructure. STM experiments were performed in an ultra-high-vacuum (UHV) chamber with a base pressure of approximately 5×10^{-11} Torr. STM and STS images were simultaneously acquired at a temperature of 100 K. Transport behaviors of BFO domain walls were measured in a manner of three-terminal architecture with source, drain and gate electrodes. All the electrodes were made of gold and bonded with copper wires for standard electrical measurements. The measurements of magnetic hysteresis loops were performed at room temperature using a MicroMag vibrating sample magnetometer (VSM) 3900 (Princeton Measurements

Cooperation). Magneto-transport measurements were operated at 4 K *via* quantum design physical property measurement system (PPMS) using a standard four-probe method.

Acknowledgements

This work was supported by the National Science Council of Republic of China (under contract no. NSC-101-2119-M-009-003-MY2), Ministry of Education (grant no. MOE-ATU 101W961), and Center for Interdisciplinary Science at National Chiao Tung University. Prof. R. Huang is supported by Shanghai Pujiang talents plan (Grant no. 11PJ1402900). Dr C. C. Hung and Dr S. H. Chen acknowledge the financial support of Southern Taiwan Science Park under contract no. 102CC01. We would like to thank Dr R. K. Vasudevan for his help in manuscript discussion. Jan-Chi Yang and Chao-Hui Yeh contributed equally to this work.

Notes and references

1 J. Mannhart and D. G. Schlom, *Science*, 2010, **327**, 1607.
2 Y. Tokunaga, N. Furukawa, H. Sakai, Y. Taguchi, T. Arima and Y. Tokura, *Nat. Mater.*, 2009, **8**, 558.
3 A. Ohtomo and H. Y. Hwang, *Nature*, 2003, **427**, 423.
4 Y. H. Hsieh, J. M. Liou, B. C. Huang, C. W. Liang, Q. He, Q. Zhan, Y. P. Chiu, Y. C. Chen and Y. H. Chu, *Adv. Mater.*, 2012, **24**, 4564.
5 N. Reyren, S. Thiel, A. D. Caviglia, L. F. Kourkoutis, G. Hammerl, C. Richter, C. W. Schneider, T. Kopp, A.-S. Rüetschi, D. Jaccard, M. Gabay, D. A. Muller, J.-M. Triscone and J. Mannhart, *Science*, 2007, **317**, 1196.
6 J. Seidel, L. W. Martin, Q. He, Q. Zhan, Y.-H. Chu, A. Rother, M. E. Hawkridge, P. Maksymovych, P. Yu, M. Gajek, N. Balke, S. V. Kalinin, S. Gemming, F. Wang, G. Catalan, J. F. Scott, N. A. Spaldin, J. Orenstein and R. Ramesh, *Nat. Mater.*, 2009, **8**, 229.
7 S. Farokhipoor and B. Noheda, *Phys. Rev. Lett.*, 2012, **107**, 127601.
8 J. Seidel, P. Maksymovych, Y. Batra, A. Katan, S.-Y. Yang, Q. He, A. P. Baddorf, S. V. Kalinin, C.-H. Yang, J.-C. Yang, Y.-H. Chu, E. K. H. Salje, H. Wormeester, M. Salmeron and R. Ramesh, *Phys. Rev. Lett.*, 2010, **105**, 197603.
9 S. Thiel, G. Hammerl, A. Schmehl, C. W. Schneider and J. Mannhart, *Science*, 2006, **313**, 1942.
10 A. D. Caviglia, S. Gariglio, N. Reyren, D. Jaccard, T. Schneider, M. Gabay, S. Thiel, G. Hammerl, J. Mannhart and J.-M. Triscone, *Nature*, 2008, **456**, 624.
11 A. Brinkman, M. Huijben, M. Van Zalk, J. Huijben, U. Zeitler, J. C. Maan, W. G. Van Der Wiel, G. Rijnders, D. H. A. Blank and H. Hilgenkamp, *Nat. Mater.*, 2007, **6**, 493.
12 Y. H. Hsieh, E. Strelcov, J. M. Liou, C. Y. Shen, Y. C. Chen, S. V. Kalinin and Y. H. Chu, *ACS Nano*, 2013, **7**, 8627.
13 T. Zhao, A. Scholl, F. Zavaliche, K. Lee, M. Barry, A. Doran, M. P. Cruz, Y. H. Chu, C. Ederer, N. A. Spaldin, R. R. Das, D. M. Kim, S. H. Baek, C. B. Eom and R. Ramesh, *Nat. Mater.*, 2006, **5**, 823.
14 Y.-H. Chu, L. M. Martin, M. B. Holcomb, M. Gajek, S. J. Han, Q. He, N. Balke, C. H. Yang, D. Lee, W. Hu, Q. Zhan, P. L. Yang, A. Fraile-Rodriguez, A. Scholl, S. X. Wang and R. Ramesh, *Nat. Mater.*, 2008, **7**, 478.
15 Q. He, C. H. Yeh, J. C. Yang, G. Singh-Bhalla, C. W. Laing, P. W. Chiu, G. Catalan, L. W. Martin, Y. H. Chu, J. F. Scott and R. Ramesh, *Phys. Rev. Lett.*, 2012, **108**, 067203.
16 A. Lubk, S. Gemming and N. A. Spaldin, *Phys. Rev. B: Condens. Matter Mater. Phys.*, 2009, **80**, 104110.
17 G. Catalan, J. Seidel, R. Ramesh and J. F. Scott, *Rev. Mod. Phys.*, 2012, **84**, 119.
18 J. C. Yang, Q. He, S. J. Suresha, C. Y. Kuo, C. Y. Peng, R. C. Haislmaier, M. A. Motyka, G. Sheng, C. Adamo, H. J. Lin, Z. Hu, L. Chang, L. H. Tjeng, E. Arenholz, N. J. Podraza, M. Bernhagen, R. Uecker, D. G. Schlom, V. Gopalan, L. Q. Chen, C. T. Chen, R. Ramesh and Y. H. Chu, *Phys. Rev. Lett.*, 2012, **109**, 247606.
19 G. K. Williamson and W. H. Hall, *Acta Metall.*, 1953, **1**, 22.
20 K. Brinkman, T. Iijima and H. Takamura, *Jpn. J. Appl. Phys.*, 2007, **46**, L93.
21 J. Nogués and I. K. J. Schuller, *J. Magn. Magn. Mater.*, 1999, **192**, 203.
22 L. W. Martin, Y. H. Chu, M. B. Holcomb, M. Huijben, P. Yu, S. J. Han, D. Lee, S. X. Wang and R. Ramesh, *Nano Lett.*, 2008, **8**, 2050.
23 T. C. Schulthess and W. H. Butler, *Phys. Rev. Lett.*, 1998, **81**, 4516.
24 R. Mallik, E. V. Sampathkumaran and P. L. Paulose, *Appl. Phys. Lett.*, 1997, **71**, 2385.
25 S. S. P. Parkin, *Appl. Phys. Lett.*, 1987, **63**, 1987.
26 S. Y. Yang, J. Seidel, S. J. Byrnes, P. Shafer, C. H. Yang, M. D. Rossell, P. Yu, Y. H. Chu, J. F. Scott, J. W. Ager III, L. M. Martin and R. Ramesh, *Nat. Nanotechnol.*, 2010, **5**, 143.
27 Y. P. Chiu, Y. T. Chen, B. C. Huang, M. C. Shih, J. C. Yang, Q. He, C. W. Liang, J. Seidel, Y. C. Chen, R. Ramesh and Y. H. Chu, *Adv. Mater.*, 2011, **23**, 1530.